

THM analysis of a soil drying test in an environmental chamber: The role of boundary conditions

Agustín Cuadrado^a, Abdallah Najdi^a, Alberto Ledesma^{a,b,*}, Sebastià Olivella^{a,b}, Pere C. Prat^a

^a Dept. of Civil and Environmental Engineering, Universitat Politècnica de Catalunya-BarcelonaTech (UPC), Spain

^b CIMNE, Barcelona, Spain

ARTICLE INFO

Keywords:

Desiccating cracks
THM analysis
Environmental chamber
Unsaturated soils
Suction

ABSTRACT

This paper presents the numerical analysis of an experimental soil drying test carried on an initially slurry soil specimen with controlled temperature and relative humidity in a laboratory environmental chamber. The imposed drying conditions lead to evaporation and a consequent soil shrinkage, triggering a perimeter crack between soil body and mould. The numerical analysis follows a THM approach with two objectives: to identify the soil parameters that govern drying, and to determine the influence of the perimeter crack on evaporation. Identifying the boundary condition requires defining the vapour and heat fluxes, the corresponding transfer coefficients, and the influence of the perimeter crack. The simulations are provided in 3 separate blocks with gradually added complexity until a good fit with the experimental data is obtained. The approach signifies the importance of accounting for the mechanical problem, the initial self-weight settlements of the slurry, the wind effect in the chamber and the evaporation from the exposed crack surface. The local atmosphere within the formed crack, however, differs from the surface, requiring the use of different vapour transfer coefficients at the distinct surfaces. The simulations were assessed based on the ability to reproduce the water loss, developing suction profile and soil relative humidity.

1. Introduction

Shrinkage and cracking in drying soils is a relatively well-known phenomenon that modifies the soil's mechanical and hydraulic behaviour (Costa et al. 2018; Rodríguez et al. 2007; Yesiller et al. 2000). Much of the research about desiccation cracking has been dedicated to investigate the morphology of the cracking pattern (Kodikara et al. 2000; Konrad and Ayad 1997a; Morris et al. 1992). Some authors attributed crack initiation to heterogeneity and developing tensile stresses at the drying soil surface (Abu-Hejleh and Znidarcic 1995; Konrad and Ayad 1997b; Trabelsi et al. 2012). In many cases, the cracking problem has been studied from the fracture mechanics point of view (Amarasiri and Kodikara 2013; Amarasiri et al. 2011; Ávila 2004; Lakshmikantha 2009; Wei et al. 2020). However, despite the efforts, it remains difficult to create a consensus or definite theoretical formulation on the mechanism of crack initiation and propagation, given the nonlinearity and the large number of parameters that control the problem (Costa et al. 2013; Péron et al. 2009; Shin and Santamarina 2011; Tang et al. 2011).

The interaction occurring at the soil surface with the overlying atmosphere leads to soil water evaporation or condensation. The soil-

atmosphere interaction controls the drying process and thus the atmospheric behaviour has to be adequately simulated by means of the boundary conditions. However, this practice is not widespread in geotechnical analysis due to the lack of knowledge and complexity associated (Blight 1997; Smits et al. 2012). Changes in gradients of the overlying atmospheric variables (i.e. humidity, wind, radiation and temperature) have a direct impact on the energy available for water evaporation and soil heating, which in turn modifies the behaviour of the atmosphere in contact with the soil surface. The subsequent coupled interactions at the interface are induced by the state of the soil as well. The formation of a dry layer near the surface hinders the evaporation process, often requiring the use of diffusion resistance factors to adapt the calculated flows to the measurements (Camillo and Gurney 1986; Kondo et al. 1990; van de Griend and Owe 1994). The thickness of the diffusion zone, on the other hand, controls the soil's capacity to supply water towards the evaporation front (Lehmann et al. 2008; Shahraeni et al. 2012).

Some authors indicate that surface cracks can modify the interface, suggesting an effect on the drying process and the evaporation rate (Cui et al. 2013; Song et al. 2016). However, detailed analysis of some cracking tests leads to opposite conclusions of unaffected evaporation rates (Tang et al. 2011), and decreased rates in other instances (Song

* Corresponding author.

<https://doi.org/10.1016/j.compgeo.2021.104495>

Received 17 March 2021; Received in revised form 17 July 2021; Accepted 30 September 2021

0266-352X/© 2021 The Authors. Published by Elsevier Ltd. This is an open access article under the CC BY-NC-ND license

(<http://creativecommons.org/licenses/by-nc-nd/4.0/>).

Nomenclature

List of symbols

w is the gravimetric water content

\mathbf{u} is the displacements vector

ω_α^i is the mass fraction of a species i in a phase α

J_α^i is the flux of a species i in a phase α

T_s is the soil surface temperature

T_a is the air temperature

ρ_α is the phase density

P_α is the phase pressure

β_g is the gas transfer coefficient

γ_e is the sensible heat transfer coefficient

M_i is the molecular weight of a species

r_a is the aerodynamic resistance

r_s is the surface resistance

k is the von Kármán's Constant

z_0 is the soil roughness length

z is the wind measurement altitude

\bar{U} is the mean horizontal wind velocity

D_a is the water vapour diffusivity in air

j_e is the boundary energy flux

C_a is the volumetric heat capacity of air

ν is the Poisson's ratio

ϕ is the soil porosity

e is the void ratio

∇ is the divergence operator

s is the soil total suction

p' is the mean effective stress

S_α is the phase saturation degree

γ_D is the soil dry density

k_{ra} is the phase relative permeability

\mathbf{k} is the intrinsic permeability tensor

τ is the tortuosity

κ_α is the phase thermal conductivity

λ is van Genuchten's retention curve shape parameter

h_e is the latent heat of evaporation

Table 1
Soil basic properties.

Physical property	Experimental value
Sand content (≤ 2 mm)	46.8%
Silt content (≤ 63 μm)	42.7%
Clay content (≤ 2 μm)	10.5%
ρ_s (solid particles density)	2.71 g/cm ³
w_h (hygroscopic water content)	2.2%
w_l (liquid limit)	32%
PI (plasticity index)	16%

et al. 2016). Nevertheless, there is an associated difficulty of experimentally quantifying the evaporation from distinct parts of the soil surface, leading to indefinite conclusions. As cracks create new interfaces for soil-atmosphere interaction, it seems logical to simulate first their impact on the drying process.

Some researchers have carried out numerical analyses of desiccating soils, but their works focus mainly on the simulation of crack openings, with little attention to boundary conditions (Asahina et al. 2014; Levatti et al. 2019; Tran et al. 2019). To cope with the discontinuities some authors use mesh fragmentation techniques (Sánchez et al., 2014), the discrete element method (Gui et al., 2016) or Voronoi tessellations (Gui et al., 2018) incorporating a damage-elastic cohesive fracture law (Vo et al., 2017). However, experiments suggest that soil shrinkage and cracking are very much dependent on boundary conditions, which are difficult to implement in the analyses (Cuadrado et al. 2019; Lakshmikantha et al. 2018, Zeng et al., 2020). This work concentrates on the numerical boundary conditions that should be considered in the simulations, particularly when a crack is formed. For this purpose, a numerical model is constructed considering the coupled soil-atmosphere interactions at the initial boundary condition and at the subsequent interfaces at the crack openings.

An experimental test (Lakshmikantha 2009) that was carried in an environmental chamber at the laboratories of the Technical University of Catalonia (UPC) is simulated numerically. The soil specimen, prepared at initial slurry conditions, was placed in a cylindrical mould of 40 cm diameter and 10 cm height. During drying, the specimen separated from the mould, creating only a border gap but no surface cracks. However, this border gap is commonly referred to as a "perimeter crack" (Cordero et al. 2020). Therefore, distinct boundary conditions can be applied at the top surface and at the vertical perimeter crack surfaces.

The paper presents the experimental results of the desiccation test with a background of the used environmental chamber and the Barcelona silty-clay soil used. Applied physical atmospheric variables are translated into numerical boundary conditions. Meanwhile, a constitutive approach is adopted to capture the involved coupled Thermo-Hydro-Mechanical processes. The numerical results are presented against the physical data from the laboratory test, demonstrating a good fit with increased level of model complexity.

2. Materials and testing

The Barcelona silty-clay has been extensively studied for its hydro-mechanical properties (Mora-Ortiz, 2016; Barrera 2002; Gens et al. 1995). The soil is a clayey silt with about 10% of clay and a substantial amount of silt and sand. However, according to the Unified Soil Classification System (USCS) this soil is classified as a low plasticity clay (CL). A summary of basic soil properties is shown in Table 1.

The drying test was executed in an existing environmental chamber at the UPC laboratory (Fig. 1), designed for soil desiccation tests (Lakshmikantha 2009). The relative humidity (RH) can be imposed on soil specimens using a dehumidifier (DST-Seibu Giken RECUSORB DR-010B) that injects dry air while collecting wet air. Temperature (T) was maintained using infrared lamps that were activated as temperature dropped below the designated 35 °C. The soil specimen was prepared at 30% initial gravimetric water content, and dry density $\gamma_D = 1510$ kg/m³, in the 40–10 cm cylindrical mould instrumented with different sensors (Fig. 2a). Sensors marked T1-T4 are UMS T5 tensiometers, inserted into the soil body at different depths to capture the suction development profile up until 100 kPa. The Vaisala® HMP-230 hygrometers (V1 and V2) measuring the soil relative humidity and temperature were placed at their location through the lateral boundary ten days after drying initiation, when the specimen started desaturating following cavitation of the tensiometers. The specimen ensemble was placed over 3 load cells (SSM) to capture weight fluctuations, attributed to soil water loss.

3. Interpretation of experimental results

The final state of the soil specimen after 45 days (1080 h) of drying exhibits a perimeter crack, developed between 80 and 280 h from test initiation, reaching 1 cm thickness separating the soil body from the mould (Fig. 2a). Fig. 2b shows the image of the flipped specimen, taken after test termination, where cracks that developed at the bottom surface

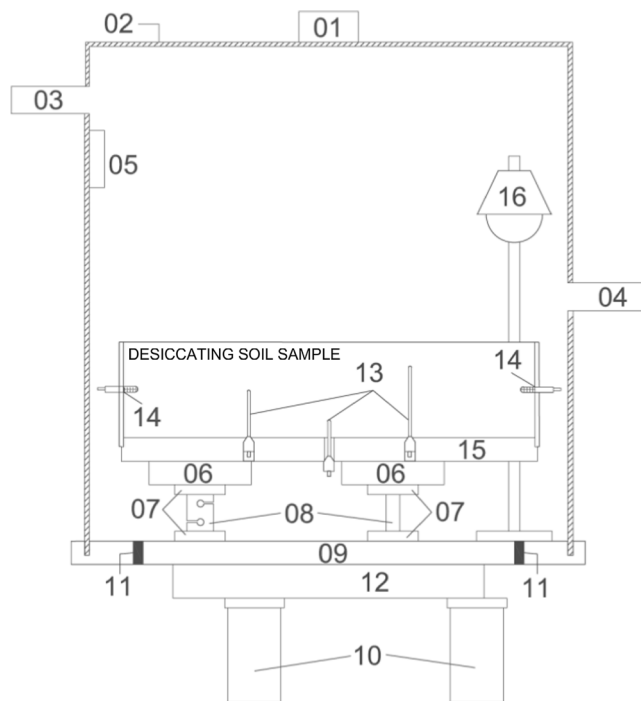
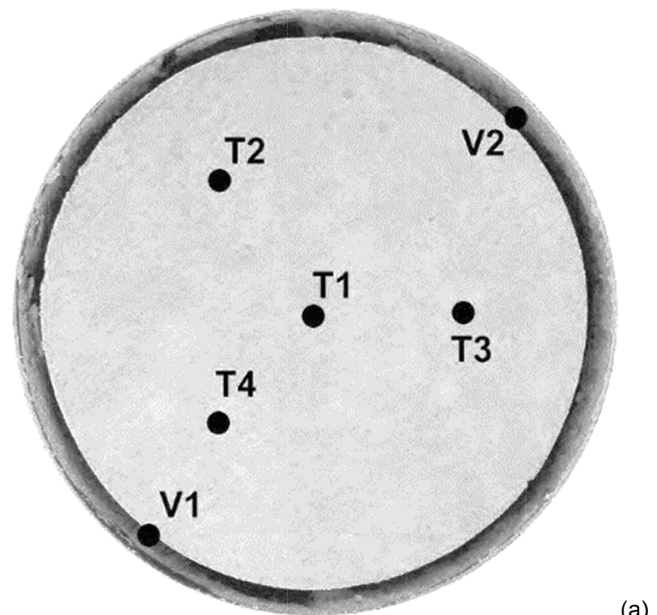


Fig. 1. Environmental chamber diagram (modified from Lakshmikantha 2009): (1) digital camera; (2) clear chamber cover ($1.5 \times 1 \times 1$ m); (3) air outlet; (4) air inlet; (5) chamber temperature and relative humidity measurements; (6) load cells supports for the mould; (7) load cell insulators; (8) load cells; (9) chamber base; (10) chamber base supports; (11) wiring holes; (12) metal ring to distribute the load; (13) tensiometers at different depths (UMS T5); (14) soil relative humidity and temperature sensors (Vaisala HMP-230); (15) specimen mould; (16) infrared lamps to regulate temperature.

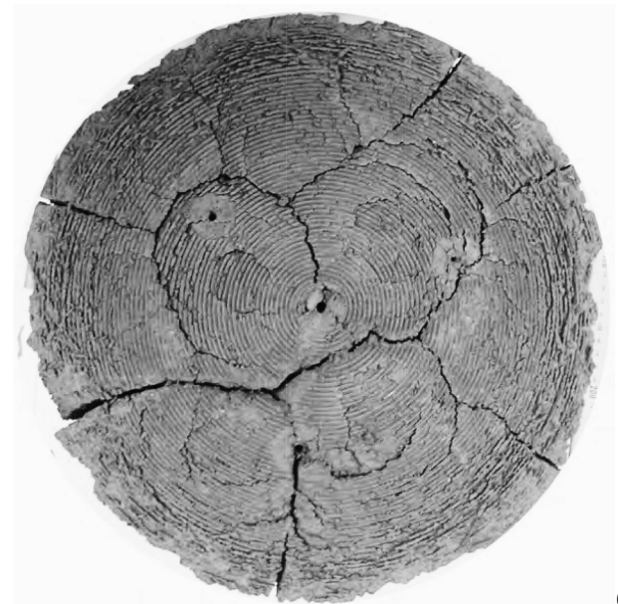
can be seen. These cracks did not emerge to the top surface, remaining unexposed to the environmental conditions. The arrangement of sensors may influence the pattern of cracks, but indeed there is evidence that cracks may initiate at the bottom boundary. Several papers present experiments supporting this fact (i.e., Lakshmikantha et al., 2018; Zeng et al., 2020; Zaidi et al., 2021). Bottom cracks have also been found in clay sediments in nature (Weinberger, 1999). The reason for that is the constraint or friction that the lower boundary imposes on the desiccating soil (either the tray bottom in the laboratory or another soil or rock layer in the field). Additionally, the specimen experienced curling (Nahlawi and Kodikara 2002), where near the outer perimeter the soil detached from the mould bottom. The lack of internal cracks reaching the upper surface provided the advantage of eliminating associated uncertainties of quantifying evaporation from within a complex crack network, allowing the application of a homogeneous boundary condition to simulate soil-atmosphere interaction. Another advantage is the existence of the perimeter crack between soil and mould, with a well-defined geometry that allows the application of boundary conditions on the lateral, vertical surface.

3.1. Environmental chamber measurements

The value of the relative humidity was maintained close to 40% during the first 25 days, dropping below that target value between days 25 and 45 (Fig. 3). Temperature on the other hand remained constant at about 35 °C, except for days 7 to 9 where it dropped to 30 °C. However, a simplified constant value of 35 °C has been used in the numerical simulations for the whole period.



(a)



(b)

Fig. 2. Specimen at end of the test: (a) top soil surface with location of the sensors; (b) bottom cracked surface.

3.2. Sensor Measurements

The three stages of evaporation from a bare soil, subjected to stationary meteorological conditions (such as in the environmental chamber) with no water supply from a shallow water table, can be related to the evolution of the gravimetric water content (Hillel 2004). These stages can be seen in Fig. 4, that shows measurements from the Vaisala sensor V2. For graphical clarity, results from sensor V1 (which are similar) are omitted. The first stage lasts 18 days, with an approximately linear descent indicating a constant initial evaporation rate. At this stage, the suction gradient growth as soil dries compensates for the reduction of hydraulic conductivity caused by the decrease of the voids' volume. Water supply is then maintained at the soil surface, meeting the evaporative demand of the chamber atmosphere. The shrinkage-induced perimeter crack at this stage does not affect the constant slope of the water-loss curve. The second stage lasts between days 18 and 26, when the moisture content evolution slope declines. Evaporation reduces due to limited availability of soil-water supply to the surface, and the

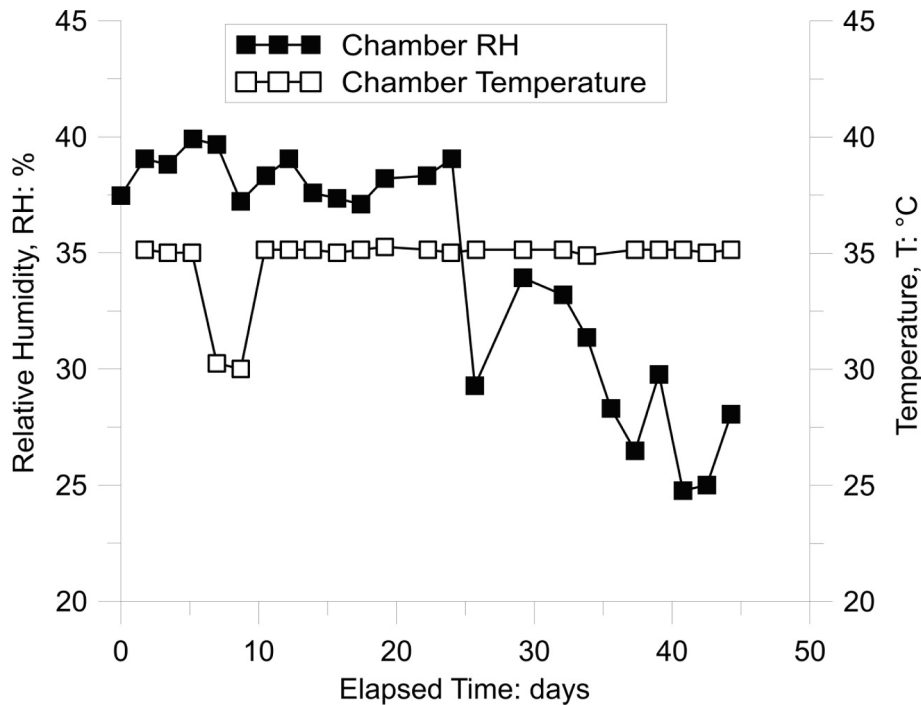


Fig. 3. Evolution of relative humidity and air temperature inside the environmental chamber.

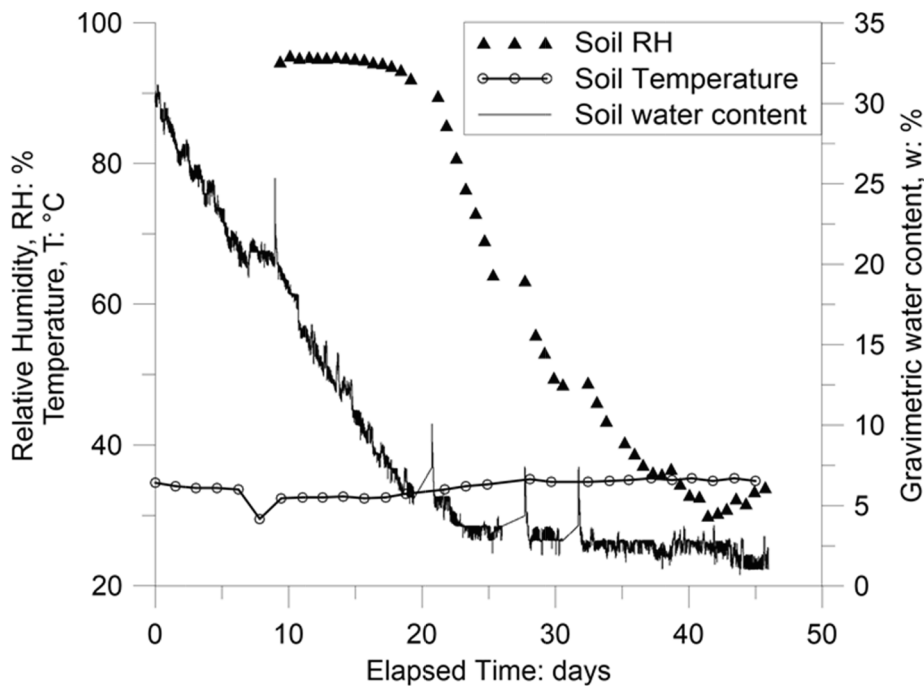


Fig. 4. Evolution of gravimetric water content, soil specimen relative humidity and temperature.

dominant flow changes from advective to diffusive. Third and last stage starts at day 26 up until test termination. The slope of the gravimetric water content curve slowly decreases, reaching a final value of 2%. The soil becomes very dry and the evaporation rate is close to zero. Obtained readings serve as a trend rather than exact soil RH-values, due to suspected loss of sensor-soil contact as a result of the ensuing shrinkage.

Fig. 5 shows the suction values measured by tensiometers T2-T4 (values from T1 are omitted for graphical clarity). The suction measurements show a homogeneous profile during the early drying stage. Although moisture content was decreasing, suction remained at a range

between 0 and 14 kPa during the first 4 days, indicating near-saturation conditions. This is a key aspect to understanding the mechanical behaviour of the specimen. Matric suction increased thereafter up to 90 kPa at day 10, just when tensiometers reached cavitation.

3.3. Internal wind circulation

The internal horizontal wind circulation created by the dehumidifier had a direct impact on the evaporation rate, and needs to be quantified accordingly. Wind speed was not measured in the original test, so the

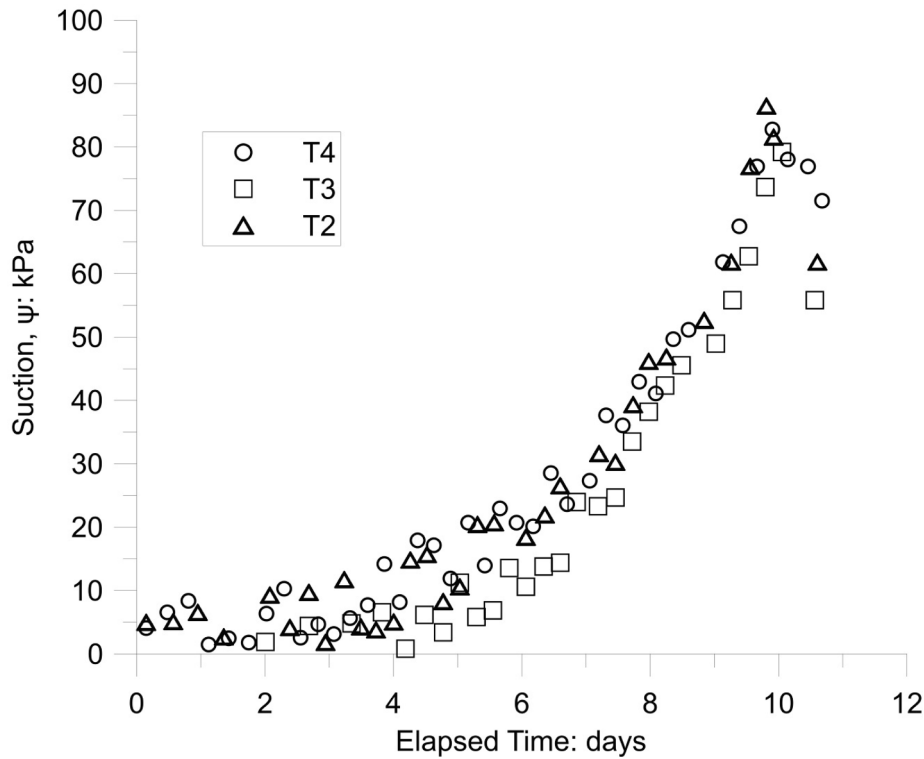


Fig. 5. Suction values measured by tensiometers T2-T4.

atmospheric conditions were recreated inside the environmental chamber. A high-precision sonic anemometer DS-2 (DECAGON) was mounted on an adjustable tripod to take readings at different altitudes from the specimen surface (Fig. 6). The recorded average (\bar{U}) and maximum (U') wind speed values are given in Table 2. Since gust speeds reach double the average speed, wind turbulence is expected to influence vapour diffusion, favouring advective fluxes.

4. Numerical model

Simulations are performed using the finite element software CODE_BRIGHT v.5.4 (Gens and Olivella 2001; Olivella et al. 1994; Olivella et al. 1995). The theoretical framework consists of a multiphase and multispecies approach. Phases are identified by subscripts (*s*: solid, *l*: liquid, *g*: gas) and species by superscripts (*w*: water, *a*: dry air). The formulation is based on 3 components: balance equations, constitutive equations, and equilibrium constraints. The state variables (unknowns) are: displacements in each direction, \mathbf{u} (m); liquid pressure P_l (MPa); gas pressure P_g (MPa); and soil temperature T (°C).

4.1. Balance equations

Mass balance equations are established per species rather than phases following the compositional approach (Olivella et al. 1994; Olivella et al. 1995). The solid mass balance is written in terms of the porosity ϕ as state variable, while the liquid mass balance is written in terms of the unknown liquid pressure P_l . The displacements \mathbf{u} are the main variables for the momentum balance, and the equation is reduced to the equilibrium of total stresses. The mass movement fluxes are defined separately in terms of advective $\mathbf{j}_{E\alpha}$ ($\alpha = s, l, g$) and non-advective \mathbf{i} fluxes. Finally, the internal energy balance equation is expressed considering the internal energy of each phase E_α ($\text{J m}^{-2} \text{s}^{-1}$) and assuming thermal equilibrium between phases and the temperature as state variables. Having an externally-applied atmospheric temperature in this case did not eliminate the internal temperature fluctuations

occurring due to the heat fluxes between the porous system and the atmosphere.

4.2. Constitutive equations and equilibrium constraints

A set of constitutive equations links the balance equations unknowns (e.g., P_l) to the dependent variables (e.g., S_l) (Table 3).

The water vapour concentration in the gaseous phase (ρ_g^w) is in equilibrium with the liquid phase through the psychrometric law:

$$\rho_g^w = (\rho_g^w)^0 \exp \left[\frac{-(P_g - P_l)M_w}{R(273.15 + T)\rho_l} \right] \quad (1)$$

where $(P_g - P_l)$ is the suction (MPa); M_w is the water molecular weight ($0.018 \text{ kg mol}^{-1}$); R is the universal gas constant ($8.314 \text{ J mol}^{-1} \text{ K}^{-1}$); and $(\rho_g^w)^0$ is the saturated volumetric mass content of vapour in the gaseous phase in equilibrium with a flat surface of water at the same temperature, calculated as:

$$(\rho_g^w)^0 = \frac{M_w P_{v(T)}}{R(273.15 + T)} \quad (2)$$

where $P_{v(T)}$ (MPa) is the saturated vapour pressure. In case of pure water, it is calculated in terms of the temperature T (°C):

$$P_{v(T)} = 136075 \exp \left[\frac{-5239.7}{(273.15 + T)} \right] \quad (3)$$

Darcy's law represents the advective flow of the liquid phase with respect to the solid phase:

$$\mathbf{q}_l = - \frac{\mathbf{k}k_{rl}}{\mu_l} (\nabla P_l - \rho_l \mathbf{g}) \quad (4)$$

where \mathbf{g} is the gravity vector, μ_l (Pa s) is the dynamic viscosity of the liquid phase; \mathbf{k} (m^2) is the intrinsic permeability tensor computed in terms of the porosity using Kozeny's model for a continuum medium (Eq.8); and k_{rl} is the liquid phase relative permeability defined



Fig. 6. Anemometer mounted inside the environmental chamber for wind measurements under test conditions similar to the original by Lakshmikantha (2009).

Table 2

Wind measurements in the central axis of the environmental chamber showing the vertical measurement height above the soil surface (z); the number of measurements taken (N); the average wind speed (\bar{U}) and the mean burst speed (U') recorded.

z (cm)	N	\bar{U} (m s ⁻¹)	U' (m s ⁻¹)
10	19	0.1	0.2
60	18	0.1	0.2
70	24	0.3	0.5
80	14	0.2	0.3

separately in terms of the effective liquid saturation S_e and the shape parameter λ , Eq. (7) (van Genuchten 1980), often providing a satisfactory representation at laboratory scale (Cai et al. 2014).

$$k = k_0 \frac{\phi^3}{(1-\phi)^2} \frac{(1-\phi_0)^2}{\phi_0^3} \quad (5)$$

$$k_{rl} = \sqrt{S_e} \left[1 - (1 - S_e^{1/\lambda})^2 \right]^2 \quad (6)$$

The suction versus degree of saturation relation (soil–water retention curve) is fitted to the experimental data using the well-known van Genuchten (1980) model.

Table 3

Equilibrium and constitutive equations state variables.

	Law	State variable	Eq. No.
Balance equations	Mass balance of solid	Porosity	ϕ (Olivella et al. 1994; Olivella et al. 1995)
	Mass balance of water	Liquid pressure	P_l
	Momentum balance	Displacements	\mathbf{u}
	Energy balance	Temperature	T
Equilibrium	Psychrometric Law	Vapour concentration in gas	ρ_g^w [1]
Constitutive	Darcy's Law	Liquid advective flux	\mathbf{q}_l [4]
	Retention Curve	Degree of saturation	S_l [7]
	Fick's Law	Non-advective vapour flux	\mathbf{i}_g^w [8]
	Fourier's Law	Conductive heat flux	\mathbf{i}_c [12]

$$S_e = \frac{S_l - S_{rl}}{S_{ls} - S_{rl}} = \left[1 + \left(\frac{P_g - P_l}{P} \right)^{\frac{1}{1-\lambda}} \right]^{-\lambda}; P = P_0 \frac{\sigma}{\sigma_0} \quad (7)$$

where S_l , S_{rl} and S_{ls} are the current, residual and maximum degrees of saturation, respectively; P_0 (MPa) is the air entry value at a reference temperature; and σ_0 and σ (N m⁻¹) are the surface tensions at the reference and actual temperatures, respectively. In this work, $S_{ls} = 1$, $S_{rl} = 0$, and parameters P_0 and λ are fitted for best match with the given soil experimental data points (Barrera, 2002). The intrinsic permeability has been adopted from experimental measurements as well (Barrera, 2002; Mora-Ortiz, 2016).

Non-advective fluxes generally embrace molecular diffusion and mechanical dispersion, calculated using Fick's law. The molecular diffusion of vapour in the gaseous phase is calculated in terms of the gas saturation degree S_g , and the temperature:

$$\mathbf{i}_g^w = -\mathbf{D}_g^w \nabla \omega_g^w = -(\phi \rho_g S_g \tau D_m^w \mathbf{I}) \nabla \omega_g^w \quad (8)$$

where τ is the tortuosity, \mathbf{I} is the identity matrix, \mathbf{D}_g^w is the dispersion tensor; and D_m^w (m² s⁻¹) is the dispersion coefficient corresponding to the molecular diffusion of vapour in air

$$D_m^w = 5.9 \times 10^{-12} \frac{(273.15 + T)^{2.3}}{P_g} \quad (9)$$

The tortuosity can be assigned a constant value or computed in terms of the liquid's degree of saturation:

$$\tau = \tau_0 \quad (10)$$

$$\tau = A(1 - S_l)^m \quad (11)$$

where A and m are parameters controlling the diffusion gradient.

Heat conduction is expressed by Fourier's law in terms of the global porous medium's thermal conductivity κ (J m⁻¹ s⁻¹ K⁻¹).

$$\mathbf{i}_c = -\kappa \nabla T \quad (12)$$

The thermal conductivity is a complex parameter involving the three phases of the soil. The approximation used for its calculation is given by the dry ($\kappa_{dry} = 0.243$) and saturated ($\kappa_{sat} = 1.448$) conductivity values (W m⁻¹ K⁻¹) obtained from the literature for similar soils (Farouki 1986; Oke 1987).

$$\kappa = \kappa_{sat} \sqrt{S_l} + \kappa_{dry} (1 - \sqrt{S_l}) \quad (13)$$

Table 4
Boundary conditions for Block A.

Parameter	Eq.	Upper			Lateral			Bottom		
		A1	A2	A3	A1	A2	A3	A1	A2	A3
$(\rho_g)^0$	16	1.1308			0		1.1308	0		
$(\omega_g^w)^0$	18	0.0139					0.0139			
T^0 (°C)	19	35					35	35		
β_g	26	10^3	0.001				0.001	0		
γ_e	27	10^3	1				1	10^3		

Table 5
Constitutive equation parameters for Block A.
(¹) Retention curve parameters; (²) Intrinsic permeability; (³) Tortuosity.

P_0 (¹) (MPa)	0.05
λ (¹)	0.26
k_0 (²) (m ²)	10^{-14}
τ_0 (³)	1

4.3. Boundary conditions

The boundary conditions can be defined in terms of the main variables or their derivatives (i.e. a fixed suction value or a fixed water flux applied to the soil surface). Soil-atmosphere interaction can be simulated by applying a time-dependent exponential soil suction profile at the soil interface (Vo et al. 2019). Experiments suggest that above the soil surface most of the boundary variables exhibit high gradients which complicate the definition of a constant value as boundary condition (Cordero et al. 2021; Lozada et al. 2019). It is therefore more convenient to impose a flux boundary condition at the soil surface for water and energy transfer.

The general form of the hydraulic boundary condition in the numerical model is obtained by adding fluxes at the nodes. For drying problems, the boundary conditions reduce to vapour (\mathbf{j}_g^w) and heat (\mathbf{j}_{Es}) fluxes. Vapour flux through the boundary is composed of 3 distinct terms.

$$j_g^w = (\omega_g^w)^0 j_g^0 + (\omega_g^w)^0 \gamma_g (P_g^0 - P_g) + \beta_g \left[(\rho_g \omega_g^w)^0 - \rho_g \omega_g^w \right] \quad (14)$$

where the superscript “0” denotes prescribed atmospheric values; P_g is the gas pressure; j_g^0 is a prescribed gas flux; and γ_g and β_g are transfer coefficients controlling the magnitude of interactions, to be determined. The first term corresponds to a vapour flux imposed by gas injection; the second, the advective vapour flux due to pressure difference; and the third, the diffusive vapour flux due to difference in prescribed concentrations. In the particular case of drying, and considering constant gas pressure (equal to atmospheric pressure: $P_g = P_a = 0.1$ MPa), the boundary condition becomes

$$j_g^w = \beta_g \left[(\rho_g \omega_g^w)^0 - \rho_g \omega_g^w \right] \quad (15)$$

where ρ_g is the gas density approximated from the molecular weight of dry air ($M_a = 0.029$ kg mol⁻¹); and ω_g^w is the vapour mass fraction in the air. Their product results in the vapour density:

$$\rho_g^0 = \frac{P_a M_a}{R(273.15 + T)} \times 10^6 \quad (16)$$

Normally, the molecular weight of air is the sum of dry air and vapour. However, since the maximum weight of vapour that air can sustain is comparably small with that of dry air, the error is negligible

and the calculation is simplified. The relative humidity is defined as the ratio between vapour concentration and saturated vapour. The atmospheric vapour density ρ_v is computed from the imposed relative humidity RH , knowing the saturated vapour density (Eq. (2)).

$$\rho_v = \rho_v^{sat} \cdot RH \quad (17)$$

Finally, the vapour mass fraction in the air $(\omega_g^w)^0$ (kg kg⁻¹) is obtained:

$$(\omega_g^w)^0 = \frac{\rho_v}{\rho_g^0} \quad (18)$$

Following this approach, the transfer coefficient β_g acquires the physical meaning of vapour diffusion coefficient at the soil-atmosphere interface. As for energy fluxes at the interface, following a similar scheme to the vapour flux, the boundary condition is reduced to imposed temperature changes:

$$j_e = j_e^0 + \gamma_e (T^0 - T) \quad (19)$$

where j_e^0 is the imposed heat flux and γ_e is the heat transfer coefficient. In this case, γ_e acts as a thermal diffusion coefficient at the soil-atmosphere interface.

4.4. Surface energy balance equation

The boundary condition must reproduce the atmospheric behaviour inside the environmental chamber. To this end, the well-known surface energy balance equation (EBS) is used (Blight 1997):

$$R_n = H + LE + G \quad (20)$$

This equation represents the soil-atmosphere interactions at the interface through four energy flows: absorption or emission of electromagnetic radiation through the surface (net radiation, R_n); the thermal conduction between soil surface and atmosphere (sensible heat, H); energy required for soil water evaporation or vapour condensation on the surface (latent heat, LE) and heat conduction responsible for altering the soil body temperature (heat flow, G). In this particular study, the test was carried in closed laboratory conditions with negligible radiation interference. The atmospheric gradients of sensible and latent heat flows condition the evaporative demand. These flows are given by

$$H = \frac{C_a(T_s - T_a)}{r_h} \quad (21)$$

$$LE = \frac{h_e(\rho_s - \rho_a)}{r_a + r_s} \quad (22)$$

where T_s and T_a (K) are temperatures of the soil surface and air, respectively; C_a is the volumetric heat capacity of air calculated as: $C_a = \rho_a \cdot C_p$, where ρ_a is the dry air density at room temperature (1.168 kg m⁻³) and $C_p = 1005$ J kg⁻¹ K⁻¹ is the specific heat capacity, typically around 1200 J m⁻³ K⁻¹ (Stull 1988; Wallace and Hobbs 2006); ρ_s is the air density at the soil surface; h_e is the latent heat of evaporation (J

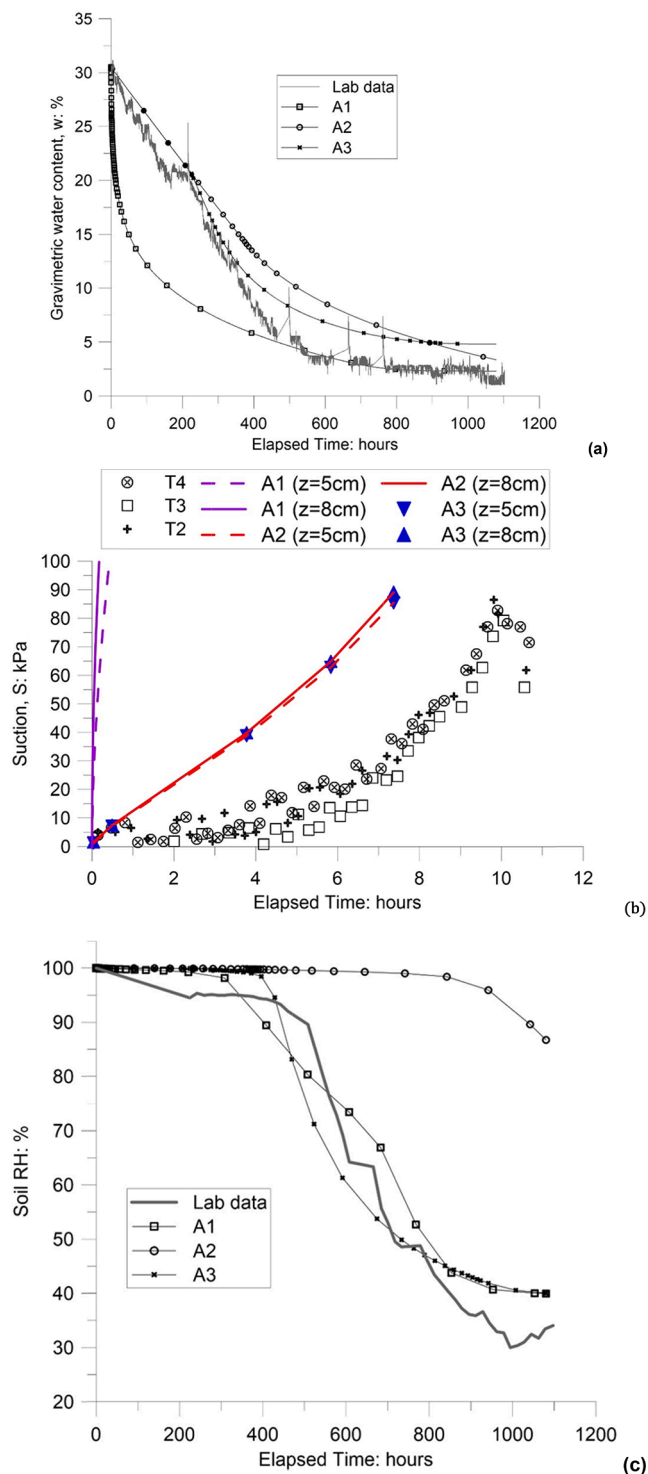


Fig. 7. Block A numerical results: (a) gravimetric water content; (b) matrix suction; (c) soil relative humidity.

kg^{-1}); r_s is the soil surface resistance to evaporation; and r_h and r_a are aerodynamic resistance factors governing water vapour and temperature dispersion into atmosphere. The average wind speed behaviour inside the chamber does not fit the logarithmic profile as it does on bare, flat and open grounds (Campbell and Norman 1998; Hillel 2004). Therefore, the use of aerodynamic resistances is an approximation. These factors have been expressed by many authors with satisfactory results (Camillo et al. 1983; Cui et al. 2013; Saito et al. 2006; Yamanaka et al. 1997). Generally, it has been observed that the two factors are used

interchangeably and considered equal (Garratt 1977; Joffre 1982). A dimensional analysis is carried to obtain the corresponding units for sensible and latent heat flows ($\text{J m}^{-2} \text{s}^{-1}$), leading to the resistance factors (s m^{-1}):

$$r_h = r_a = \frac{1}{k^2 \bar{U}} \left[\ln \frac{z}{z_0} + \psi_H(\zeta) \right] \left[\ln \frac{z}{z_0} + \psi_M(\zeta) \right] \quad (23)$$

where von Kármán constant $k = 0.41$ is assumed (Tagesson 2012); z is the measuring altitude of the atmospheric variables; $z_0 = 0.001 \text{ m}$ is an assumed value of roughness length, a usual value for bare smooth soil surfaces (Šimůnek et al. 2013); and $\psi_{H,M}(\zeta)$ are atmospheric stability factors for heat flux (H) and for momentum flux (M). The term ζ is a dimensionless atmospheric stability parameter that depends on the Monin-Obukhov length: a relation between shear stress created by wind and buoyancy of air by convection to produce turbulent kinetic energy (Monin and Obukhov 1954; Obukhov 1971). In other words, it is a measure of convective behaviour of the atmosphere represented by the so-called stability condition, or a measure of the atmospheric resistance to air displacement by convection as explained below.

The resistance of a volume of air to move vertically depends on the difference in density between such volume and that of the surrounding air. If the surrounding air is less dense, the volume tends to rise leading to convection currents that transport heat and humidity. The mixing capacity of heat and humidity depends on the turbulence that is generated in this latter movement. In this sense, turbulence can be understood as a chaotic movement of air that enhances the heat and moisture exchange, either between layers of air, or between the soil surface and the atmosphere. Therefore, the stability condition is a measure of how that atmosphere tends to favour or suppress the turbulence that conditions the heat and humidity flow from the ground.

In general, atmospheric stability can be categorized into three distinct types: unstable, neutral, and stable. The unstable condition appears when the soil surface is warmer than the overlying layer of air in contact with the surface. The air then heats up, producing thermal updrafts that cause an increase in turbulence and in mixing heat and moisture. In the neutral condition, the temperature of the soil surface and of the air layer are similar and thus the convection is weak. Finally, in the stable condition, the air temperature is higher than at the ground surface and convection tends to be suppressed. Consequently, the stability factors increase diffusion in the unstable atmosphere, reduce it in stable conditions and have no effect in the neutral condition. In this study, as shown in Figs. 3 and 4, the atmospheric and soil temperatures are similar. The stability factors can then be ignored and the aerodynamic resistance becomes

$$r_h = r_a = \frac{1}{k^2 \bar{U}} \left[\ln \frac{z}{z_0} \right]^2 \quad (24)$$

The expression of the aerodynamic resistance comes from the field of micrometeorology. The semi-empirical log-wind-speed law has been found to fit satisfactorily experimental wind speed data, not only in the first 100 m above ground, but also directly above bare soil surfaces (Poulsen et al. 2018). More details can be found in the literature (Foken 2008; Stull 1988; Wallace and Hobbs 2006). In summary, aerodynamic resistance comes from the similarity theory to reproduce turbulent behaviour through mean values of atmospheric variables. For simulations, the best fit was achieved with chamber measurements $\bar{U} = 0.3 \text{ m s}^{-1}$ at altitude $z = 70 \text{ cm}$ above the soil surface (see Table 2).

Surface resistance to evaporation r_s (Eq. (22)) represents the vapour diffusion difficulty above the evaporation front. Vapour passing through the dry layer is not necessarily in equilibrium with moisture content of the pores, and the use of a surface resistance term is required (Bitelli et al. 2008; Camillo and Gurney 1986; Kondo et al. 1990). Many authors have obtained empirical expressions in terms of the water present at the soil's upper layer. Some authors have suggested that a linear expression for the volumetric water content at the first centimetre below the surface

Table 6

Conversion of measured atmospheric variables in the chamber into prescribed vapour mass fraction and gas density for the imposed boundary condition.

t (h)	$(\omega_g^w)^0$	$(\rho_g)^0$	t (h)	$(\omega_g^w)^0$	$(\rho_g)^0$	t (h)	$(\omega_g^w)^0$	$(\rho_g)^0$
0.0	0.0132	1.1213	334.4	0.0132	1.1213	769.8	0.0117	1.1224
41.8	0.0137	1.1209	376.2	0.0131	1.1214	811.6	0.0110	1.1228
81.9	0.0137	1.1210	418.0	0.0130	1.1214	853.4	0.0099	1.1235
125.4	0.0140	1.1207	459.8	0.0134	1.1212	895.2	0.0093	1.1240
167.2	0.0140	1.1208	532.9	0.0135	1.1211	937.0	0.0105	1.1232
209.0	0.0131	1.1214	576.5	0.0137	1.1209	978.8	0.0087	1.1244
252.5	0.0135	1.1211	616.5	0.0103	1.1233	1020.6	0.0088	1.1243
292.6	0.0137	1.1209	700.1	0.0119	1.1222	1062.4	0.0098	1.1236

Table 7

Boundary conditions for Block B.

Parameter	Eq.	Upper			Lateral			Bottom		
		B1	B2	B3	B1	B2	B3	B1	B2	B3
$(\rho_g)^0$	16	Table 6			Table 6		1.1308	0		
$(\omega_g^w)^0$	18	Table 6			Table 6		0.0139			
T^0 (°C)	19	35			35		35	35		
β_g	26	0.0012			Table 8		0.001	0		
γ_e	27	1.4571			10		1	10 ³		

Table 8

Sequential crack segments activation time.

Lateral Segments	$t_{activation}$ (h)	β_g (B1)	β_g (B2)
	81.9	0.0012	0.0004
	125.4		
	167.2		
	167.2		
	252.5		
	252.5		
	252.5		
	292.6		

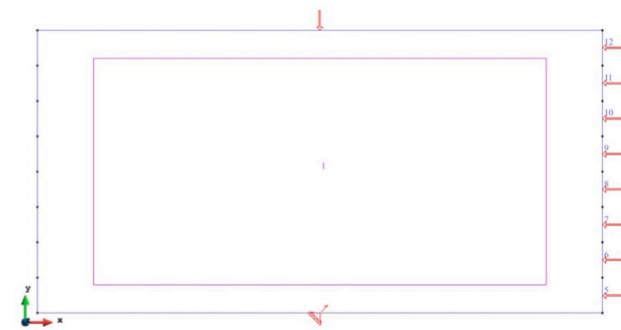


Table 9

Updated parameters for Block B. Fick's law variable tortuosity, Eq. (11).

A	8
m	3

is enough to reduce errors and evaporation corrections (Camillo and Gurney 1986), while others propose a potential expression at the first two centimetres below surface in open-air evaporation tests (Kondo et al. 1990). Based on chamber tests with air circulation, van de Griend and Owe (1994) propose two expressions depending on the volumetric content of the first surface centimetre: exponential if it is less than 15%, and constant if greater. In all expressions, resistance increases as surface humidity reduces. Surface resistance has been widely used, although its uniqueness is still highly debated. Each expression has been obtained from specific evaporation conditions and its application in models presents mismatches with observed measurements. Bitelli et al. (2008) implemented a coupled thermo-hydraulic model and concluded that, of the three surface resistance expressions analysed (Camillo and Gurney 1986; Sun 1982; van de Griend and Owe 1994), that of van de Griend

and Owe (1994) presented the best fit of their study:

$$r_s = 10 \exp[35.63(0.15 - \theta_0)] \tag{25}$$

where θ_0 is the volumetric water content at the first surface centimetre. In this study, the specimen is initially slurry with volumetric water content higher than 15%. Thus, a constant value of $r_s = 10 \text{ s m}^{-1}$ has been adopted in boundary condition calculations.

The transfer coefficient β_g , necessary to impose the vapour flux boundary condition (Eq. (15)), is derived by comparing against the latent heat LE (Eq. (22)).

$$\beta_g \left[(\rho_g \omega_g^w)^0 - \rho_g \omega_g^w \right] = \frac{(\rho_s - \rho_a)}{r_a + r_s} \rightarrow |\beta_g| = \frac{1}{r_a + r_s} \tag{26}$$

where $(\rho_g \omega_g^w)^0$ is the equivalent to atmospheric vapour density ρ_a , and $\rho_g \omega_g^w$ is the equivalent to air density at the soil surface ρ_s . On the other hand, the heat transfer coefficient γ_e , necessary to impose the reduced energy flux at the interface (Eq. (19)), is derived by comparing against the sensible heat H (Eq. (21)).

$$\gamma_e (T^0 - T) = \frac{C_a (T_s - T_a)}{r_h} \rightarrow |\gamma_e| = \frac{C_a}{r_h} \tag{27}$$

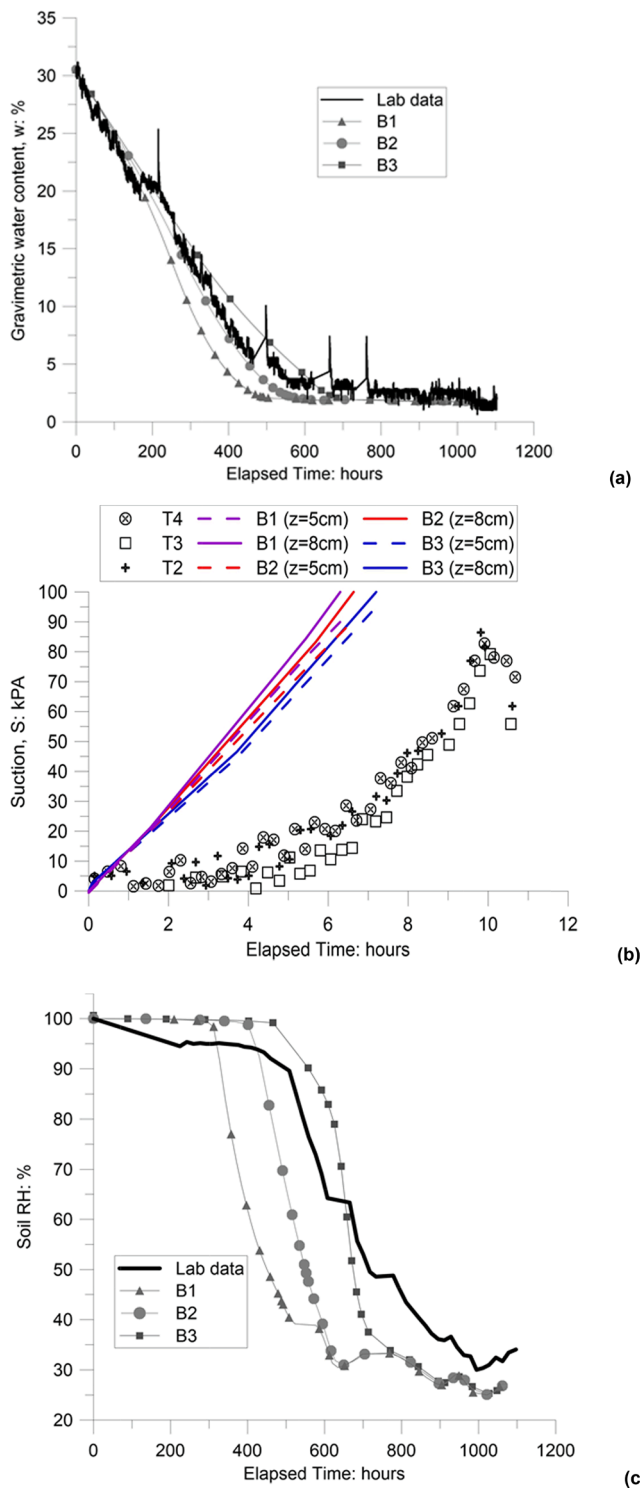


Fig. 8. Block B numerical results: (a) gravimetric water content; (b) matrix suction; (c) soil relative humidity.

here T^0 is the equivalent to atmospheric temperature T_a , and T is the equivalent to soil surface temperature T_s .

5. Numerical simulations

An axisymmetric (around the y-axis) rectangular cross-section was structured to replicate the 3D cylindrical specimen problem, assuming global homogeneous isotropic conditions. A structured mesh was

assigned (750 elements; 816 nodes), with quadrilateral-type elements, and the mesh refined near the boundaries. The bottom boundary restricts vertical movements only. Simulation results are presented in 3 blocks (A, B, C) at an increasing order of added complexity, where each block consists of 3 distinct simulations.

5.1. Block A

In the first block, the boundary condition is made constant over time as a first approximation to drying in the chamber. Allocated values in each simulation (A1, A2, A3) are presented in Table 4 for the 3 boundaries: upper (specimen surface), lateral (perimeter crack opening), and lower (mould bottom). The measured chamber wind values are not taken into account in this block, and β_g is manually assigned a constant value, which is $\beta_g = 10^3$ in simulation A1, indicating a very high diffusion gradient at the interface, where equilibrium is reached rapidly due to the forced diffusion, and $\beta_g = 0.001$ in simulations A2 and A3, indicating a low diffusion gradient with a delay in reaching equilibrium. Null values indicate no interactions (impermeable boundary). Consequently, the lateral boundary was made impermeable in the first 2 simulations (A1, A2), assuming no soil-atmosphere interactions at the perimeter crack surface. In the third simulation (A3), the atmosphere at the lateral boundary was assumed equal to the atmosphere at the upper surface. At this boundary, a temperature equal to the chamber temperature was imposed (Table 4). The bottom boundary was considered impervious in all cases. Table 5 shows the constitutive equations parameters used in Block A.

Fig. 7 shows the obtained simulation results compared against experimental measurements: (a) soil moisture content evolution; (b) matrix suction measured by tensiometers shown at two tensiometer depths (5 and 8 cm) to verify the observed physical profile homogeneity; and (c) soil humidity measured by hygrometers following cavitation of the tensiometers.

In the first simulation (A1), evaporation is numerically overstated, particularly during the first 400 h. The very high transfer coefficient value assigned for β_g (10^3) versus a significantly smaller value (0.001) in simulations A2 and A3 indicates a very high diffusion gradient at the soil-atmosphere interface, thus a more rapid soil-water evaporation (Fig. 7a). As suction increases, evaporated water is promptly replaced with pore-water moving from the specimen's core. When suction (and thus soil-water drainage at the surface) is high, the pore-water flow rate cannot counterbalance the evaporation rate. As a result, the water content in the upper zone remains relatively lower than the rest of the specimen core and thus the liquid-phase relative permeability, being a function of liquid saturation degree (Eq. (6)), is lower at the surface.

Reducing the assigned transfer coefficients (A2) produces considerably lower evaporation rate and relative humidity, indicating the significance of the wind's role by means of the transfer coefficients. Soil dries faster for high winds, whilst in its absence, molecular diffusion becomes dominant and moisture loss significantly lowers. While suction development estimations are lower in this simulation, it still overstates the experimental data. Simulations exhibit suction growth since drying initiation, not capturing the constant evolution behaviour below the air entry value, observed in the first four days, when the soil was still saturated. Similar experimental behaviour has been detected in other environmental chambers drying tests on slurries (Cordero et al. 2014; Levatti et al. 2017).

In an attempt to improve the fit, evaporation was allowed from the perimeter crack surface (A3), with the same local atmosphere as at the soil surface. However, the simulated water loss was still less than the measured one. The transfer coefficient is introduced in the lateral boundary in simulation A3 only, which results in creating a lateral evaporation front and another pathway for soil-water evaporation. Although β_g is of a smaller value, its application at the lateral boundary close to the relative humidity sensor (which is placed 3 cm horizontally

Table 10
Boundary conditions for Block C.

Parameter	Eq.	Upper			Lateral			Bottom		
		C1	C2	C3	C1	C2	C3	C1	C2	C3
$(\rho_g)^0$	16	Table 6			0	Table 6		0		
$(\omega_g^w)^0$	18	Table 6			0	Table 6				
T^0 (°C)	19	35			0	35		35		
β_g	26	0.0012			0	0.0012	Table 11	0		
γ_e	27	1.4571			0	1.4571		10^3		

Table 11
Sequential crack segments activation time.

Lateral Segments	$t_{activation}$ (h)	β_g (C3)
12	81.9	0.0012
11	125.4	0.001
10	167.2	0.0006
9	167.2	0.0004
8	252.5	0.00026
7	252.5	0.00026
6	252.5	0.00026
5	292.6	0.00026

Table 12
Constitutive equation parameters for Block C. ⁽¹⁾Fick's law variable tortuosity; ⁽²⁾Nonlinear elastic mechanical model.

Parameter	C1	C2	C3
$A^{(1)}$	6	5	8
$m^{(1)}$	3		
$a_1^{(2)}$	-1		
$a_2^{(2)}$	0		
$a_3^{(2)}$	0		
$\nu^{(2)}$	0.3		
$K_{min}^{(2)}$	0.01		

away from the right-hand-side boundary into the specimen) is enough to bring about lower values of the relative humidity at the sensor measuring location in simulation A3 compared with simulation A1 (Fig. 7c). This occurred in spite of A1 having lower global water content than A3 (Fig. 7a), since the sensor position was 5 cm away from the top surface, thus closer to the lateral boundary.

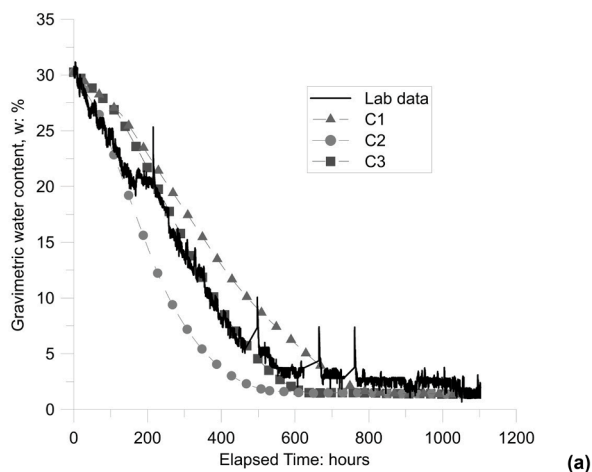
Although the results are enhanced, it seems that evaporation due to diffusion through the soil is being underestimated. For this reason, in the following blocks the tortuosity factor was modified so that it increases with the diffusive desaturation of the specimen.

5.2. Block B

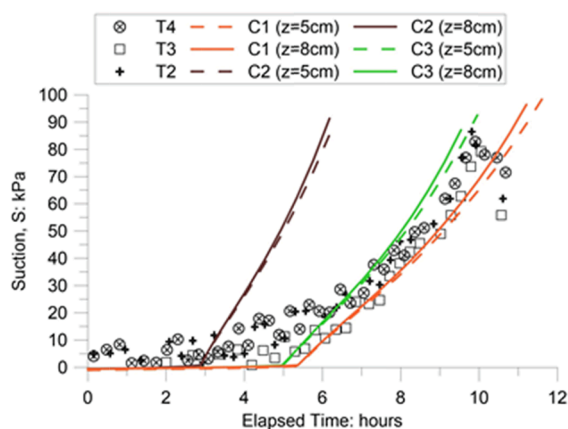
Tables 6 and 7 show the boundary conditions for the second block. The RH boundary condition is variable with time, based on relative humidity recorded at the experimental chamber (Table 6). The transfer coefficients are calculated based on best-fit wind measurements at the chamber: $\beta_g = 0.0012$ and $\gamma_e = 1.4571$. Only the first 2 simulations (B1, B2) allow for progressive opening of the perimeter crack, with the same imposed variable atmospheric conditions as at the specimen's upper surface, while no progressive opening is assumed in simulation B3. To do

that, the transfer coefficient β_g is assigned progressively along the lateral surface, to replicate the experimental descending crack propagation behaviour. For that purpose, the lateral boundary was geometrically divided into 8 equal segments where β_g for each was activated at different times (Table 8). Activation of the first segment coincides approximately with the experimentally detected crack initiation time. In simulation B1 the magnitude of the transfer coefficient is the same as at the upper specimen's surface: $\beta_{g1} = 0.0012$, while in simulation B2 it is reduced to one-third of that value: $\beta_{g2} = 0.0004$, as water evaporation rate decreases with decrease in wind speed (Song and Chen 2020). The lower value indicates different crack-atmosphere interaction from the one at the surface. Reducing the transfer coefficient in this case results in a less effective turbulent diffusion due to wind, which in turn has a significant impact on evaporation rate as has been experimentally verified (Poulsen et al. 2020).

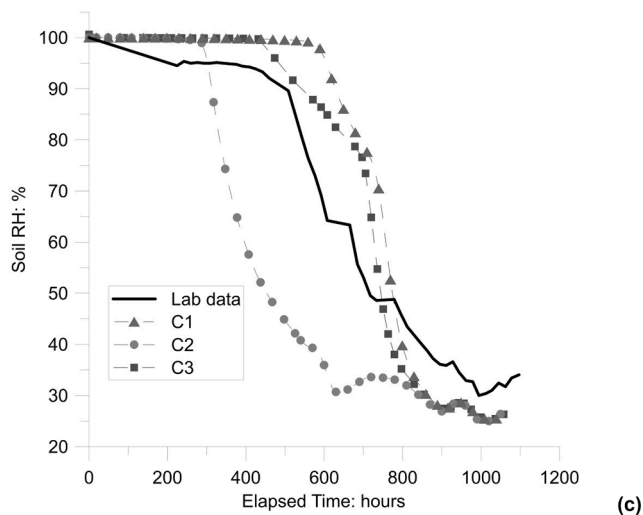
The parameters of the constitutive model are the same as in Block A, but tortuosity is made variable with the degree of saturation and depends on parameters A and m (Eq. (11), Table 9). Now the tortuosity is an exponential law that increases with the decrease of the liquid degree of saturation. With this modification, the tortuosity changes its typical unit value to become a factor enhancing the diffusivity and thus intensifies the diffusive evaporative fluxes at advanced drying stages when the advective fluxes towards the surface are no longer dominant. This change manages to reproduce the observed behaviour in many studies, although it is still a phenomenon under research. In that sense, the first studies on thermo-hydraulic coupling (Gurr et al. 1952; Taylor and Cavazza 1954) show an increase in vapour flux inside the soil compared to Fick's law predictions (Campbell and Norman 1998). The causes of diffusion improvement are two, according to Philip and de Vries (1957): (1) a condensation-evaporation mechanism in isolated areas of the liquid, and (2) a local difference of thermal conductivities increasing the gradient. According to Parlange et al. (1998), the improvement is due to convective vapour cells as a result of the soil expansion-shrinkage during the daily cycle. These hypotheses have not yet been tested (Ho and Webb, 1998; Shokri et al., 2009; Smits et al., 2012), but soil diffusion improvement has been used in numerous works to reproduce the observed measurements (Bitelli et al., 2008; Gran 2015; Han et al. 2013; Parlange et al. 1998; Saito et al. 2006; Sakai et al. 2009; Schelde et al. 1998; Smits et al. 2011). In this context, Shokri et al. (2009) managed a good fit of their evaporation tests without using a diffusion enhancing factor, providing an explanation of the physical process based on the characteristic length of Lehmann et al. (2008). This characteristic length can be interpreted as the distance in which there is ascending capillary flow from the saturation boundary to an evaporation boundary from which there is diffusion. Shokri et al. (2009) made tests with sand of several grain-sizes, using tinted water for X-ray tomography analysis. During the first stage, the liquid water raised to the surface, then evaporated and the tint deposited on the surface. In this stage, they detected, from the X-ray tomography, liquid water covering the sand grains. In a second stage, an evaporation boundary appeared that moved downward as indicated by deposition of the tint as the soil dried. This evaporation boundary is the zone reached by the liquid water because of capillarity. The distance between this boundary and the surface is where



(a)



(b)



(c)

Fig. 9. Block C numerical results: (a) gravimetric water content; (b) matrix suction; (c) soil relative humidity.

diffusion occurs. At the end of the test, they overturned the sand specimens and the area above the evaporation boundary freely disaggregated because it was fully dry. Below that boundary, the sand had some apparent cohesion and did not disaggregate. According to Shokri et al. (2009) the use of the characteristic length and Fick's law above the evaporation boundary makes unnecessary the use of diffusion enhancing factors. Nevertheless, these tests were performed on sands and there is no evidence of the applicability of those results to clays.

The results demonstrate that the adjustment of the moisture content curve improves significantly with respect to Block A in all simulations (Fig. 8). However, in simulation B1, where the latent heat transfer coefficient β_g at the lateral surface is equal to the one at the upper surface, the moisture loss is overestimated. There is an improvement in simulation B2, with that coefficient taken as one-third of the one at the upper surface. Without the influence of the perimeter crack (simulation B3), moisture loss seems insufficient. In all three cases, suction estimations do not fit the experimental measurements. Although the suction profile is no longer homogeneous throughout the soil body, the initial experimental constant evolution behaviour is not captured adequately. The lack of adjustment stems from the very fluid initial state of the soil, in a slurry consistency, and the accompanying settlements. For this reason, the mechanical analysis is included in the calculations in Block C.

5.3. Block C

The boundary conditions in this block (Table 10) were applied similarly to Block B, except for simulation C1 where no interactions are assumed at the lateral boundary. In simulation C3, the latent heat transfer coefficient β_g decreases with depth at the perimeter crack, implicating a reduction in wind magnitude effect at the deepest part of the crack. A sequential activation profile scheme similar to Block B is assumed (see Table 11).

In the constitutive equations, the mechanical calculations are now incorporated, the rest of the parameters being the same except for parameter A from the tortuosity law. Material parameters for this block are given in Table 12. A nonlinear elastic model based on stress state surfaces has been employed that describes volumetric changes due to variations in mean effective stress and suction (Alonso et al. 1990; Lloret and Alonso 1985):

$$\frac{\Delta e}{1+e} = a_1 \Delta \ln(-p') + a_2 \Delta \ln\left(\frac{s+0.1}{0.1}\right) + \left[a_3 \Delta \ln(-p') \ln\left(\frac{s+0.1}{0.1}\right) \right] \quad (28)$$

where e is the void ratio; a_1 is the coefficient that accompanies changes in mean effective stress p' (total stress plus maximum liquid or gas pressure; MPa); a_2 is the accompanying coefficient to suction changes s (gas minus liquid pressure; MPa); and a_3 is the transition coefficient between effective stress and suction. Additionally, it is necessary to input Poisson's ratio ν and minimum stiffness modulus K_{min} , a lower bound of the bulk modulus K . If a_2 and a_3 are null, suction changes do not contribute to the mechanical problem, and the bulk modulus K is calculated with this scheme:

$$d\varepsilon = a_1 d \ln(p') \rightarrow d\varepsilon = a_1 \frac{dp'}{p'} \rightarrow K = \frac{dp'}{d\varepsilon} = \frac{p'}{a_1} \quad (29)$$

where ε is the volumetric deformation. The initial fluid-like (slurry) consistency of the specimen provides an advantage of homogeneity, while making it difficult to obtain mechanical parameters.

The primary self-weight consolidation causes a thin layer of water to appear at the soil surface, and vertical shrinkage appears prior to crack initiation. A relatively high value of parameter a_1 with a low K_{min} were incorporated to reproduce the initial settling behaviour (Table 12).

Simulation results exhibit an improved adjustment in moisture loss and soil humidity (Fig. 9). The best fit was observed in the last simulation (C3) with a sequentially reduced coefficient β_g with depth. The initial suction evolution trend is captured, except in the first simulation (C1) with equal magnitude of coefficients.

Soil-atmosphere interaction at crack level is different and less compelling than at the directly exposed surface. With a smaller transfer coefficient, it appears that cracks impact on evaporation, although less than at the exposed surface, is still essential for comprehensive numerical replication. A conceptual model is proposed based on the preceding (Fig. 10), assuming minimal wind interference within the crack, but

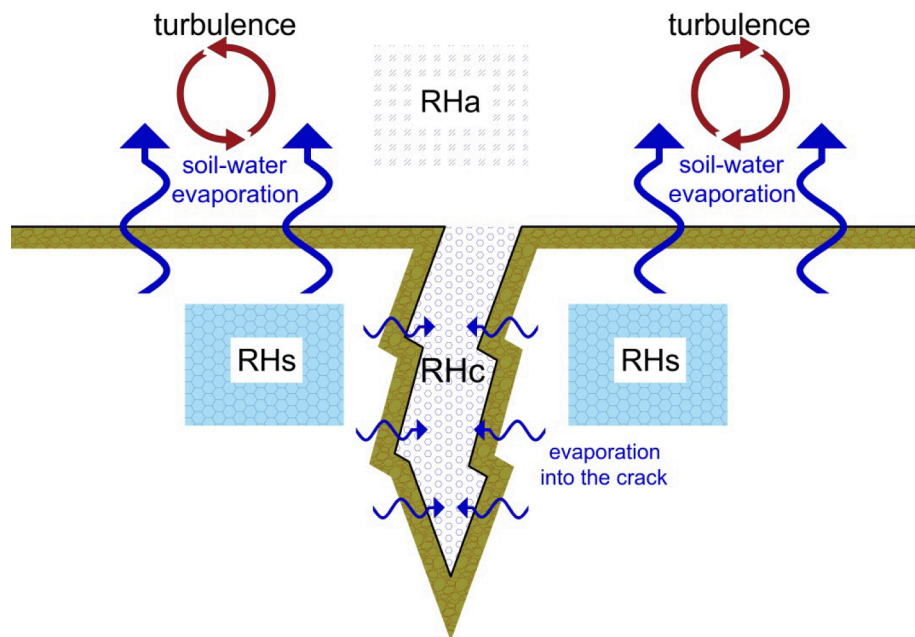


Fig. 10. Proposed conceptual model of crack internal environment. RHc: Relative humidity of the air inside the crack; RHa: Relative humidity of the open air; RHs: Relative humidity of the soil pores environment.

greater at soil surface with added turbulence effects. This causes vapour accumulation and subsequent increase of the relative humidity at the crack's internal environment, and significantly reduces the latent heat gradient. This is consistent with the experimental observations suggesting that cracking does not change significantly the evaporation rate, at least during the first stages of the desiccation (Cuadrado 2018). This is in fact one of the important points of this work and explains why cracking does not affect substantially the evaporation rate in some experiments (Tang et al., 2011), whereas it does in other cases (Cui et al., 2013). The crack delays the process of equilibration between the inner and outer suction/relative humidity. Therefore, at the beginning of the crack formation, its influence is negligible, as the inner atmosphere inside the crack is not the outer atmosphere. Eventually the crack may become almost in equilibrium with the outer atmosphere and that would increase the evaporation surface and would change the evaporation rate. Total equilibrium between the air in the crack and the outer atmosphere is difficult due to the wind, which typically is not acting inside the crack.

6. Conclusions

The simulations attempt to replicate numerically physical results of a drying experiment on a slurry specimen inside an environmental chamber. Recorded chamber atmospheric conditions are considered in the imposed numerical boundary conditions to adequately capture the experimental behaviour. For the same purpose, transfer coefficients defining the magnitude of latent and sensible heat fluxes are calculated based on chamber wind measurements. The composed constitutive model considers coupled TH processes in the first 2 blocks of simulations, and THM in the third. The numerical model assessments were carried based on 3 criteria: gravimetric water content loss, matric suction evolution for the first 10 days (until cavitation of tensiometers), and the soil's relative humidity (following the first 10 days).

The fit is improved gradually with added simulation complexity signifying the importance of considering soil-atmosphere interactions based on physically imposed relative humidity, temperature and wind values. The tortuosity is deemed an essential factor to improve desaturation by diffusion in advanced drying stages. Assigning an adequate soil-atmosphere interaction profile at the lateral boundary (perimeter crack) affects the results as well. The simulations suggest that a local

atmosphere is kept inside a crack, with an intermediate suction between the soil mass suction and the open atmospheric conditions. This effect explains why cracks do not increase significantly the surface evaporation rate, at least during the first cracking stage, and delays any change in the soil mass despite the increment of the exposed soil surface.

Finally, consideration of the initial settlement by accounting for the mechanical problem, aids in capturing the behaviour of the slurry specimen, particularly during the first days of desiccation when the soil remained saturated. Although the problem described is essentially a TH problem, incorporating the mechanical behaviour becomes essential when a slurry material is considered. This is because changes in void ratio are significant in that case and suction profiles can only be predicted if the mechanical equations are considered in the analysis.

To conclude, defining the boundary conditions in the numerical analysis of desiccating soils is a complex task. On the one hand, the experiments suggest that significant gradients of temperature and suction develop in the atmosphere close to the soil surface. On the other hand, cracks seem to create an almost closed atmosphere (i.e., not affected by wind), retarding the exchange of water vapour from the cracks to the open atmosphere. As a consequence of that, boundary conditions in this work are mostly defined in terms of prescribed fluxes, rather than prescribing values of the main variables. The analyses reveal the complexity of the soil-air interface when cracks develop and the importance of using appropriate boundary conditions to represent faithfully the physics of the processes involved.

CRediT authorship contribution statement

Agustín Cuadrado: Conceptualization, Methodology, Software, Validation, Writing – original draft. **Abdallah Najdi:** Methodology, Software, Writing – original draft. **Alberto Ledesma:** Conceptualization, Methodology, Supervision, Validation, Writing – review & editing. **Sebastià Olivella:** Software, Validation. **Pere C. Prat:** Conceptualization, Supervision, Validation, Writing – review & editing, Project administration.

Declaration of Competing Interest

The authors declare that they have no known competing financial

interests or personal relationships that could have appeared to influence the work reported in this paper.

Acknowledgements

The authors would like to acknowledge the financial support from research grants BIA2012-36498 and BIA2017-82594-R, awarded by the Spanish Ministry of Economy and Competitiveness, and the Spanish Ministry of Science, Education and Universities, respectively (both including FEDER funds, European Commission). The authors want also to thank the people at LabFerrer for their cooperation in this research, and for providing free use of the anemometer for the environmental chamber test.

References

- Abu-Hejleh, A.N., Znidarcic, D., 1995. Desiccation theory for soft cohesive soils. *J. Geotech. Eng. ASCE* 121 (6), 493–502. [https://doi.org/10.1061/\(ASCE\)0733-9410\(1995\)121:6\(493\)](https://doi.org/10.1061/(ASCE)0733-9410(1995)121:6(493)).
- Alonso, E.E., Gens, A., Josa, A., 1990. A constitutive model for partially saturated soils. *Géotechnique* 40 (3), 405–430. <https://doi.org/10.1680/geot.1990.40.3.405>.
- Amarasiri, A.L., Kodikara, J.K., 2013. Numerical modeling of desiccation cracking using the cohesive crack method. *Int. J. Geomech.* 13 (3), 213–221. [https://doi.org/10.1061/\(ASCE\)GM.1943-5622.0000192](https://doi.org/10.1061/(ASCE)GM.1943-5622.0000192).
- Amarasiri, A.L., Kodikara, J.K., Costa, S., 2011. Numerical modelling of desiccation cracking. *Int. J. Numer. Anal. Meth. Geomech.* 35 (1), 82–96. <https://doi.org/10.1002/nag.894>.
- Asahina, D., Houseworth, J.E., Birkholzer, J.T., Rutqvist, J., Bolander, J.E., 2014. Hydro-mechanical model for wetting/drying and fracture development in geomaterials. *Comput. Geosci.* 65, 13–23. <https://doi.org/10.1016/j.cageo.2013.12.009>.
- Ávila, G., 2004. Estudio de la retracción y el agrietamiento de arcillas. Aplicación a la arcilla de Bogotá. Ph.D. thesis. UPC-BarcelonaTech.
- Barrera, M., 2002. Estudio experimental del comportamiento hidro-mecánico de suelos colapsables. Ph.D. thesis. UPC-BarcelonaTech.
- Bittelli, M., Ventura, F., Campbell, G.S., Snyder, R.L., Gallegati, F., Pisa, P.R., 2008. Coupling of heat, water vapor, and liquid water fluxes to compute evaporation in bare soils. *J. Hydrol.* 362 (3–4), 191–205. <https://doi.org/10.1016/j.jhydrol.2008.08.014>.
- Blight, G.E., 1997. Interactions between the atmosphere and the Earth. *Géotechnique* 47 (4), 713–767. <https://doi.org/10.1680/geot.1997.47.4.713>.
- Cai, G., Zhou, A., Sheng, D., 2014. Permeability function for unsaturated soils with different initial densities. *Can. Geotech. J.* 51 (12), 1456–1467. <https://doi.org/10.1139/cgj-2013-0410>.
- Camillo, P.J., Gurney, R.J., 1986. A resistance parameter for bare-soil evaporation models. *Soil Sci.* 141 (2), 95–105. <https://doi.org/10.1097/00010694-198602000-00001>.
- Camillo, P.J., Gurney, R.J., Schmutge, T.J., 1983. A soil and atmospheric boundary layer model for evapotranspiration and soil moisture studies. *Water Resour. Res.* 19 (2), 371–380. <https://doi.org/10.1029/WR019i002p00371>.
- Campbell, G.S., Norman, J.M. (Eds.), 1998. *An Introduction to Environmental Biophysics*. Springer New York, New York, NY.
- Cordero, J.A., Prat, P.C., Ledesma, A., 2021. Experimental analysis of desiccation cracks on a clayey silt from a large-scale test in natural conditions. *Eng. Geol.* 292, 106256. <https://doi.org/10.1016/j.enggeo.2021.106256>.
- Cordero, J., Cuadrado, A., Ledesma, A., and Prat, P.C. 2014. Patterns of cracking in soils due to drying and wetting cycles. In 6th International Conference on Unsaturated Soils, UNSAT 2014. Edited by N. Khalili, A. Russell, and A. Khoshghalb. Sydney. Taylor and Francis, Vol.1, pp. 381–387.
- Cordero, J., Najdi, A., Encalada, D., Prat, P.C., and Ledesma, A. 2020. Experimental and numerical analysis of soil desiccating cracks in compacted and non-compacted specimens. In 4th European Conference on Unsaturated Soils (E-UNSAT 2020). Lisboa. <https://doi.org/10.1051/e3sconf/202019503021>.
- Costa, S., Kodikara, J., Shannon, B., 2013. Salient factors controlling desiccation cracking of clay in laboratory experiments. *Géotechnique* 63 (1), 18–29. <https://doi.org/10.1680/geot.9.P.105>.
- Costa, S., Kodikara, J., Barbour, S.L., Fredlund, D.G., 2018. Theoretical analysis of desiccation crack spacing of a thin, long soil layer. *Acta Geotech.* 13 (1), 39–49. <https://doi.org/10.1007/s11440-017-0602-9>.
- Cuadrado, A., 2018. THM analysis of the soil-atmosphere interaction in clay soils under drying conditions (in Spanish)thesis, UPC-BarcelonaTech.
- Cuadrado, A., Encalada, D., Ledesma, A., Prat, P.C., 2019. Soil surface boundary condition in desiccating soils. In: XVII European Soil Mechanics and Geotechnical Engineering Conference. Jarðtæknifélag Islands / Icelandic Geotechnical Society, Reykjavík, Iceland. <https://doi.org/10.32075/17ECSMGE-2019-0763>.
- Cui, Y.J., Ta, A.N., Hemmati, S., Tang, A.-M., Gatmiri, B., 2013. Experimental and numerical investigation of soil-atmosphere interaction. *Eng. Geol.* 165, 20–28. <https://doi.org/10.1016/j.enggeo.2012.03.018>.
- Farouki, O. 1986. Thermal properties of soils. Series on Rock and Soil Mechanics, Trans Tech Publications, 11: 136p.
- Foken, T., 2008. *Micrometeorology*. Springer, Berlin-Heidelberg.
- Garratt, J.R., 1977. Review of drag coefficients over oceans and continents. *Mon. Weather Rev.* 105, 915–929. [https://doi.org/10.1175/1520-0493\(1977\)105](https://doi.org/10.1175/1520-0493(1977)105).
- Gens, A., Olivella, S., 2001. THM phenomena in saturated and unsaturated porous media. *Revue Française de Génie Civil* 5 (6), 693–717. <https://doi.org/10.1080/12795119.2001.9692323>.
- Gens, A., Alonso, E.E., Lloret, A., 1995. Effect of structure on the volumetric behaviour of a compacted soil. In: First International Conference on Unsaturated Soils (UNSAT'95), pp. 83–88.
- Gran, M., 2015. Coupled heat and water flow dynamics in dry soils: Application to a multilayer waste cover. Ph.D. thesis. UPC-BarcelonaTech.
- Gui, Y., Hu, W., Zhao, Z., Xing, Z., 2018. Numerical modelling of a field soil desiccation test using a cohesive fracture model with Voronoi tessellations. *Acta Geotech.* 13 (1), 87–102. <https://doi.org/10.1007/s11440-017-0558-9>.
- Gui, Y., Zhao, Z., Kodikara, J., Bui, H., Yang, S., 2016. Numerical modelling of laboratory soil desiccation cracking using UDEC with a mix-mode cohesive fracture model. *Eng. Geol.* 202, 14–23. <https://doi.org/10.1016/j.enggeo.2015.12.028>.
- Gurr, C.G., Marshall, T.J., Hutton, J.T., 1952. Movement of water in soil due to a temperature gradient. *Soil Sci.* 74 (5), 335–346.
- Han, J., Zhou, Z., Liu, J., Zbicinski, L., Zhang, Z., 2013. Dynamics of soil water evaporation during soil drying: laboratory experiment and numerical analysis. *The Scientific World Journal* 2013. <https://doi.org/10.1155/2013/240280>.
- Hillel, D., 2004. *Introduction to Environmental Soil Physics*. Elsevier.
- Ho, C.K., Webb, S.W., 1998. Review of porous media enhanced vapor-phase diffusion mechanisms, models, and data—does enhanced vapor-phase diffusion exist? *J. Porous Media* 1 (1), 71–92. <https://doi.org/10.1615/JPorMedia.v1.i1.10.1615/JPorMedia.v1.i1.60>.
- Joffre, S.M., 1982. Momentum and heat transfers in the surface layer over a frozen sea. *Bound.-Layer Meteorol.* 24 (2), 211–229. <https://doi.org/10.1007/BF00121668>.
- Kodikara, J., Barbour, S.L., Fredlund, D.G. 2000. Desiccation cracking of soil layers. In *Unsaturated Soils for Asia*. Edited by H. Rahardjo, D.G. Toll, and E.C. Leong. 18-19 May 2000. Balkema, pp. 693–698.
- Kondo, J., Saigusa, N., Sato, T., 1990. A parameterization of evaporation from bare soil surfaces. *J. Appl. Meteorol.* 29 (5), 385–389. [https://doi.org/10.1175/1520-0450\(1990\)029](https://doi.org/10.1175/1520-0450(1990)029).
- Konrad, J.-M., Ayad, R., 1997a. Desiccation of a sensitive clay: field experimental observations. *Can. Geotech. J.* 34 (6), 929–942. <https://doi.org/10.1139/c97-063>.
- Konrad, J.-M., Ayad, R., 1997b. An idealized framework for the analysis of cohesive soils undergoing desiccation. *Can. Geotech. J.* 34, 477–488.
- Lakshminantha, M.R., 2009. *Experimental and theoretical analysis of cracking in drying soils*. PhD thesis. UPC-BarcelonaTech, Barcelona, Spain.
- Lakshminantha, M.R., Prat, P.C., Ledesma, A., 2018. Boundary effects in the desiccation of soil layers with controlled environmental conditions. *Geotech. Test. J.* 41 (4), 675–697. <https://doi.org/10.1520/GTJ20170018>.
- Lehmann, P., Assouline, S., Or, D., 2008. Characteristic lengths affecting evaporative drying of porous media. *Phys. Rev. E – Statist., Non. Soft Matt. Phys.* 77 (5), 056309. <https://doi.org/10.1103/PhysRevE.77.056309>.
- Levatti, H.U., Prat, P.C., Ledesma, A., 2017. Numerical analysis of desiccation, shrinkage and cracking in low plasticity clayey soils. In: *Computational Plasticity XIV*. Edited by E. Onate and D.R.J. Owen. Barcelona. CIMNE, pp. 268–275.
- Levatti, H.U., Prat, P.C., Ledesma, A., 2019. Numerical and experimental study of initiation and propagation of desiccation cracks in clayey soils. *Comput. Geotech.* 105, 155–167. <https://doi.org/10.1016/j.compgeo.2018.09.015>.
- Lloret, A., and Alonso, E.E. 1985. State surfaces for partially saturated soils. In XI International Conference on Soil Mechanics and Foundation Engineering. San Francisco. Balkema, pp. 557–562.
- Lozada, C., Caicedo, B., Thorel, L., 2019. A new climatic chamber for studying soil-atmosphere interaction in physical models. *Int. J. Phys. Modell. Geotech.* 19 (6), 286–304. <https://doi.org/10.1680/jphmg.17.00073>.
- Monin, A.S., Obukhov, A.M., 1954. Basic laws of turbulent mixing in the surface layer of the atmosphere. *Trans. Akad. Nauk SSSR Geofiz. Inst.* 24, 163–187.
- Mora-Ortiz, R.S., 2016. *Efectos de la microestructura en el comportamiento hidromecánico de suelos compactados*. PhD Thesis. UPC-BarcelonaTech, Barcelona, Spain.
- Morris, P.H., Graham, J., Williams, D.J., 1992. Cracking in drying soils. *Can. Geotech. J.* 29, 263–277.
- Nahlawi, H., Kodikara, J., 2002. Experimental observations on curling of desiccating clay. In: *Third International Conference on Unsaturated Soils*. Edited by J.F.T. Jucá, T.M.P. de Campos, and F.A.M. Marinho. Recife, Brasil. Balkema, Vol.2, pp. 553–556.
- Obukhov, A.M., 1971. Turbulence in an atmosphere with a non-uniform temperature. *Bound.-Layer Meteorol.* 2, 7–29.
- Oke, T.R., 1987. *Boundary layer climates*. Methuen & Co.
- Olivella, S., Carrera, J., Gens, A., Alonso, E.E., 1994. Nonisothermal multiphase flow of brine and gas through saline media. *Transp. Porous Media* 15 (3), 271–293. <https://doi.org/10.1007/BF00613282>.
- Olivella, S., Gens, A., Carrera, J., Alonso, E.E., 1995. Numerical formulation for a simulator (CODE BRIGHT) for the coupled analysis of saline media. *Eng. Computat.* 13, 87–112.
- Parlange, M.B., Cahill, A.T., Nielsen, D.R., Hopmans, J.W., Wendroth, O., 1998. Review of heat and water movement in field soils. *Soil Tillage Res.* 47, 5–10.
- Péron, H., Hueckel, T., Laloui, L., Hu, L.B., 2009. Fundamentals of desiccation cracking of fine-grained soils: experimental characterisation and mechanisms identification. *Can. Geotech. J.* 46 (10), 1177–1201. <https://doi.org/10.1139/T09-054>.
- Philip, J.R., de Vries, D.A., 1957. Moisture movement in porous materials under temperature gradients. *Trans. Am. Geophys. Union* 38 (2), 222. <https://doi.org/10.1029/TR038i002p00222>.

- Poulsen, T.G., Furman, A., Liberzon, D., 2018. Effects of near-surface wind speed and gustiness on horizontal and vertical porous medium gas transport and gas exchange with the atmosphere. *Eur. J. Soil Sci.* 69, 279–289. <https://doi.org/10.1111/ejss.12531>.
- Poulsen, T.G., Cai, W., Garg, A., 2020. Water evaporation from cracked soil under moist conditions as related to crack properties and near-surface wind speed. *Eur. J. Soil Sci.* 71 (4), 627–640. <https://doi.org/10.1111/ejss.v71.410.1111/ejss.12926>.
- Rodríguez, R.L., Sánchez, M.J., Ledesma, A., Lloret, A., 2007. Experimental and numerical analysis of a mining waste desiccation. *Can. Geotech. J.* 44, 644–658. <https://doi.org/10.1139/T07-016>.
- Saito, H., Šimůnek, J., Mohanty, B.P., 2006. Numerical analysis of coupled water, vapor, and heat transport in the vadose zone. *Vadose Zone J.* 5 (2), 784–800. <https://doi.org/10.2136/vzj2006.0007>.
- Sakai, M., Toride, N., Šimůnek, J., 2009. Water and vapor movement with condensation and evaporation in a sandy column. *Soil Sci. Soc. Am. J.* 73 (3), 707–717. <https://doi.org/10.2136/sssaj2008.0094>.
- Sánchez, M., Manzoli, O.L., Guimaraes, L.N., 2014. Modeling 3-D desiccation soil crack networks using a mesh fragmentation technique. *Comput. Geotech.* 62, 27–39. <https://doi.org/10.1016/j.compgeo.2014.06.009>.
- Schelde, K., Thomsen, A., Heidmann, T., Schjønning, P., Jansson, P.-E., 1998. Diurnal fluctuations of water and heat flows in a bare soil. *Water Resour. Res.* 34 (11), 2919–2929. <https://doi.org/10.1029/98WR02225>.
- Shahraeeni, E., Lehmann, P., Or, D., 2012. Coupling of evaporative fluxes from drying porous surfaces with air boundary layer: Characteristics of evaporation from discrete pores. *Water Resour. Res.* 48 (9) <https://doi.org/10.1029/2012WR011857>.
- Shin, H., Santamarina, J.C., 2011. Desiccation cracks in saturated fine-grained soils: particle-level phenomena and effective-stress analysis. *Géotechnique* 61 (11), 961–972. <https://doi.org/10.1680/geot.8.P.012>.
- Shokri, N., Lehmann, P., Or, D., 2009. Critical evaluation of enhancement factors for vapor transport through unsaturated porous media. *Water Resour. Res.* 45 (10) <https://doi.org/10.1029/2009WR007769>.
- Šimůnek, J., Šejna, M., Saito, H., Sakai, M., van Genuchten, M.T., 2013. The HYDRUS-1D software package for simulating the one-dimensional movement of water, heat and multiple solutes in variably-saturated media. University of California Riverside, Riverside, California, Department of Environmental Sciences.
- Smits, K.M., Cihan, A., Sakaki, T., Illangasekare, T.H., 2011. Evaporation from soils under thermal boundary conditions: experimental and modeling investigation to compare equilibrium- and nonequilibrium-based approaches. *Water Resour. Res.* 47 (5) <https://doi.org/10.1029/2010WR009533>.
- Smits, K.M., Ngo, V.V., Cihan, A., Sakaki, T., Illangasekare, T.H., 2012. An evaluation of models of bare soil evaporation formulated with different land surface boundary conditions and assumptions. *Water Resour. Res.* 48 (12) <https://doi.org/10.1029/2012WR012113>.
- Song, W.-K., Chen, Y., 2020. Modelling of evaporation from free water surface. *Geomech. Eng.* 21 (3), 237–245. <https://doi.org/10.12989/GAE.2020.21.3.237>.
- Song, W.-K., Cui, Y.-J., Tang, A.M., Ding, W.-Q., Wang, Q., 2016. Experimental study on water evaporation from compacted clay using environmental chamber. *Can. Geotech. J.* 53 (8), 1293–1304. <https://doi.org/10.1139/cgj-2015-0415>.
- Stull, R.B. (Ed.), 1988. *An Introduction to Boundary Layer Meteorology*. Springer Netherlands, Dordrecht.
- Sun, S.F., 1982. *Moisture and heat transport in a soil layer forced by atmospheric conditions*. M.Sc. thesis. University of Connecticut.
- Tagesson, T., 2012. *Turbulent transport in the atmospheric surface layer*, Report TR-12-05. Lund University, Department of Physical Geography and Ecosystem Science.
- Tang, C.-S., Shi, B., Liu, C., Suo, W.-B., Gao, L., 2011. Experimental characterization of shrinkage and desiccation cracking in thin clay layer. *Appl. Clay Sci.* 52 (1–2), 69–77. <https://doi.org/10.1016/j.clay.2011.01.032>.
- Taylor, S.A., Cavazza, L., 1954. The movement of soil moisture in response to temperature gradients. *Soil Sci. Soc. Am. J.* 18 (4), 351. <https://doi.org/10.2136/sssaj1954.03615995001800040001x>.
- Trabelsi, H., Jamei, M., Zenri, H., Olivella, S., 2012. Crack patterns in clayey soils: Experiments and modeling. *Int. J. Numer. Anal. Meth. Geomech.* 36 (11), 1410–1433. <https://doi.org/10.1002/nag.v36.1110.1002/nag.1060>.
- Tran, D.K., Ralaizafisolairivony, N., Charlier, R., Mercatoris, B., Léonard, A., Toye, D., Degre, A., 2019. Studying the effect of desiccation cracking on the evaporation process of a Luvisol – from a small-scale experimental and numerical approach. *Soil Tillage Res.* 193, 142–152. <https://doi.org/10.1016/j.still.2019.05.018>.
- van de Griend, A.A., Owe, M., 1994. Bare soil surface resistance to evaporation by vapor diffusion under semiarid conditions. *Water Resour. Res.* 30 (2), 181–188. <https://doi.org/10.1029/93WR02747>.
- van Genuchten, M.T., 1980. Closed-form equation for predicting the hydraulic conductivity of unsaturated soils. *Soil Sci. Soc. Am. J.* 44 (5), 892–898. <https://doi.org/10.2136/sssaj1980.03615995004400050002x>.
- Vo, T.D., Pouya, A., Hemmati, S., Tang, A.M., 2017. Numerical modelling of desiccation cracking of clayey soil using a cohesive fracture method. *Comput. Geotech.* 85, 15–27. <https://doi.org/10.1016/j.compgeo.2016.12.010>.
- Vo, T.D., Pouya, A., Hemmati, S., Tang, A.M., 2019. Modelling desiccation crack geometry evolution in clayey soils by analytical and numerical approaches. *Can. Geotech. J.* 56 (5), 720–729. <https://doi.org/10.1139/cgj-2018-0105>.
- Wallace, J.M., Hobbs, P.V., 2006. *Atmospheric Science: An Introductory Survey*. Elsevier.
- Wei, X., Gao, C., Liu, K.e., 2020. A review of cracking behavior and mechanism in clayey soils related to desiccation. *Adv. Civil Eng.* 1–12. <https://doi.org/10.1155/2020/8880873>.
- Weinberger, R., 1999. Initiation and growth of cracks during desiccation of stratified muddy sediments. *J. Struct. Geol.* 21 (4), 379–386.
- Yamanaka, T., Takeda, A., Sugita, F., 1997. A modified surface-resistance approach for representing bare-soil evaporation: wind tunnel experiments under various atmospheric conditions. *Water Resour. Res.* 33 (9), 2117–2128. <https://doi.org/10.1029/97WR01639>.
- Yesiller, N., Miller, C.J., Inci, G., Yaldo, K., 2000. Desiccation and cracking behavior of three compacted landfill liner soils. *Eng. Geol.* 57 (1–2), 105–121. [https://doi.org/10.1016/S0013-7952\(00\)00022-3](https://doi.org/10.1016/S0013-7952(00)00022-3).
- Zaidi, M., Ahfir, N.-D., Alem, A., Taibi, S., El Mansouri, B., Zhang, Y., Wang, H., 2021. Use of X-ray computed tomography for studying the desiccation cracking and self-healing of fine soil during drying and wetting paths. *Eng. Geol.* 292 <https://doi.org/10.1016/j.enggeo.2021.106255>.
- Zeng, H., Tang, C.-S., Cheng, Q., Zhu, C., Yin, L.-Y., Shi, B., 2020. Drought-induced soil desiccation cracking behaviour with consideration of basal friction and layer thickness. *Water Resources Research*, 56, e2019WR026948. <https://doi.org/10.1029/2019WR026948>.